Unlocking Li_2CO_3-Li_2SO_4 as Cathodes for Li-ion Batteries

Authors: Mingliang Yu[1], Bo Li[2], Jing Wang[3], Yaobin Xu[4], Nan Zhang[5], Min Soo Jung[1], Zhichen Xue[6], Yukio Cho[7], Min-Jae Kim[8], Guangxia Feng[9], Yufei Yang[9], Alexis Scida[1], Yiming Sui[1], Zengqing Zhuo[8], Mu-huai Lu[1], Ankit Kumar Yadav[1], Kyriakos C. Stylianou[1], Wanli Yang[8], Yijin Liu[10], Chongmin Wang[4], Thomas Osborn Popp[1], Chunsheng Wang[5,*], Tongchao Liu[3,*], Xueli Zheng[7,9,*], De-en Jiang[2,*], Xiulei Ji[1,*]

Affiliations:

[1]Department of Chemistry, Oregon State University; Corvallis, Oregon, 97331, United States.

[2]Department of Chemical and Biomolecular Engineering, Vanderbilt University; Nashville, Tennessee, 37235, United States.

[3]Chemical Sciences and Engineering Division, Argonne National Laboratory; Lemont, Illinois, 60439, United States.

[4]Environmental Molecular Sciences Laboratory, Pacific Northwest National Laboratory, Richland, Washington, 99354, United States.

[5]Department of Chemical and Biomolecular Engineering, University of Maryland; College Park, Maryland, 20742, United States.

[6]Stanford Synchrotron Radiation Light Source, SLAC National Accelerator Laboratory, Menlo Park, California, 94025, United States.

[7]Applied Energy Division, SLAC National Accelerator Laboratory; Menlo Park, California, 94025, United States.

[8]Advanced Light Source, Lawrence Berkeley National Laboratory; Berkeley, California, 94720, United States.

[9]Materials Science and Engineering, Stanford University; Stanford, California, 94305, United States.

[10]Walker Department of Mechanical Engineering, The University of Texas at Austin, Austin, Texas, 78712, United States.

*Corresponding authors. Emails: david.ji@oregonstate.edu (X.J.), de-en.jiang@vanderbilt.edu (D.J.), xuelizh8@stanford.edu (X.L.), liut@anl.gov (T.L), cswang@umd.edu (C.W.)

Amidst the rapid expansion of the electric vehicle industry, the need for alternative battery technologies that balance economic viability with sustainability has never been more critical. Here, we report that common lithium salts of Li_2CO_3 and Li_2SO_4 are transformed into cathode active mass in Li-ion batteries by ball milling to form a composite with Cu_2S. The optimal composite cathode comprising Li_2CO_3, Li_2SO_4, and Cu_2S, with a practical active mass loading of 12.5-13.0 mg/cm^2, demonstrates a reversible capacity of 247 mAh/g based on the total mass of Cu_2S and the lithium salts, a specific energy of 716 Wh/kg, and a stable cycle life. This cathode chemistry rivals layered oxide cathodes of Li-ion batteries in energy density but at substantially reduced cost and ecological footprint. Mechanistic investigations reveal that in the composite both Li_2CO_3 and Li_2SO_4 serve as the active mass, Li_2SO_4 enhances kinetic properties and reversibility, and Cu_2S stabilizes the resulting anionic radicals for reversibility as a binding agent. Our findings pave the way for directly using lithium salts as cathodes for Li-ion batteries to meet the ever-increasing market demands sustainably.

Currently, the most energetic power batteries for electric vehicles (EVs) are Li-ion batteries (LIBs) that utilize layered transition metal oxides as the cathodes. These cathodes rely on Ni and Co as redox centers and structural anchors[1,2], where Ni and Co not only drive up the cost of LIBs—with the cathode materials accounting for over 50% of the total cell cost—but face a looming supply shortage that could halt the EV industry[3,4]. In parallel with developments in lithium metal anode[5,6,7] and solid-state electrolytes[8,9] for LIBs with much greater energy density, it is pivotal to explore

alternative cathode chemistries for sustainable electrified transportation. Although notable advances have been made via the topotactic intercalation compounds free of Co and Ni, these compounds have limitations: the olivine $LiFe_{1-x}Mn_xPO_4$[10,11,12] do not offer competitive energy density, and the Li-rich metal oxides are plagued by the rapid capacity fading and voltage sagging[13,14,15,16,17]. Meanwhile, non-metal elemental cathodes, including sulfur[18,19,20,21,22], oxygen[23,24,25], and halogens[26,27,28], while offering promising energy densities, still await breakthroughs for practical applications.

What species can serve as redox centers of electrodes in LIBs? Traditionally, species like transition metal ions and elemental substances, known for their well-defined oxidation states, have been considered[29]. However, inorganic polyanions, the building blocks of minerals, are typically considered redox-inert. One exception is the carbonate ion of Li_2CO_3, which anodically decomposes into CO_2 and O_2 irreversibly, thus allowing Li_2CO_3 to serve as a lithium-replenishing agent in cathodes of LIBs[30,31]. This raises a critical question: Can the anodic oxidation of Li_2CO_3 be transformed reversible, thus enabling it to be a viable cathode material? Herein, we report that the answer is yes and both Li_2CO_3 and Li_2SO_4 exhibit reversible electrochemical redox behaviors when finely mixed with Cu_2S, which acts as a binding agent. The composite of Li_2CO_3, Li_2SO_4, and Cu_2S exhibits a specific energy and stable cycle life comparable to the expensive layered oxide cathodes. Here, the common lithium salts[32,33] that are usually consumed as precursors in the manufacturing of other lithium compounds directly serve as the cathode active mass. This new cathode chemistry not only reduces the carbon footprint associated with the cathode manufacturing but opens new avenues for achieving higher energy densities.

Cu_2S-lithium-salt composite cathodes

Intuitively, Li_2CO_3 and Li_2SO_4 might seem unsuitable as battery electrode materials due to their electronically and ionically insulating properties[34]. Moreover, their anodic oxidation, if it occurs, may produce unstable anionic radicals[35,36]. Can an electronically conductive agent facilitate their reversible anodic oxidation if this agent binds the resulting anionic radicals, e.g., CO_3^{x-} and SO_4^{x-} ($0 < x < 2$)? To test this possibility, we selected Cu_2S as a binding agent, a naturally occurring conducting mineral that requires minimal processing. To enable the interfacing between Cu_2S and lithium salts, the Cu_2S phase is thoroughly mixed with the lithium salts using ball milling (see Methods), resulting in composites containing Li_2CO_3, Li_2SO_4, and Cu_2S, at the molar ratios of 1:1:0, 2:0:1, 0:2:1, and 1:1:1, respectively. Each composite is supplemented with a carbon additive (KetjenBlack, or KB) (5.9 wt.%) to further improve the conductivity, and is denoted as LCS, CuLC, CuLS, and CuLCS, respectively. X-ray diffraction (XRD) patterns show that composites with a single lithium salt—CuLC and CuLS—display diffraction peaks: broadened peaks for Li_2CO_3 in CuLC and distinguishable peaks for Li_2SO_4 in CuLS (**Supplementary Figs. 1a,b**). In contrast, both LCS and CuLCS show completely amorphous structures (**Supplementary Figs. 1c,d**). Scanning electron microscopy (SEM) images show that the composites consist of micron-sized particles (**Supplementary Figs. 2a, 3a** and **4a**), maintaining a morphology similar to that of precursors (**Supplementary Fig. 5**). The transmission electron microscopy (TEM) and corresponding energy-dispersive X-ray spectroscopy (EDS) results reveal the uniform dispersion of pertinent elements at the nanoscale, attesting the thorough mixing of amorphous phases (**Supplementary Figs. 2–4**).

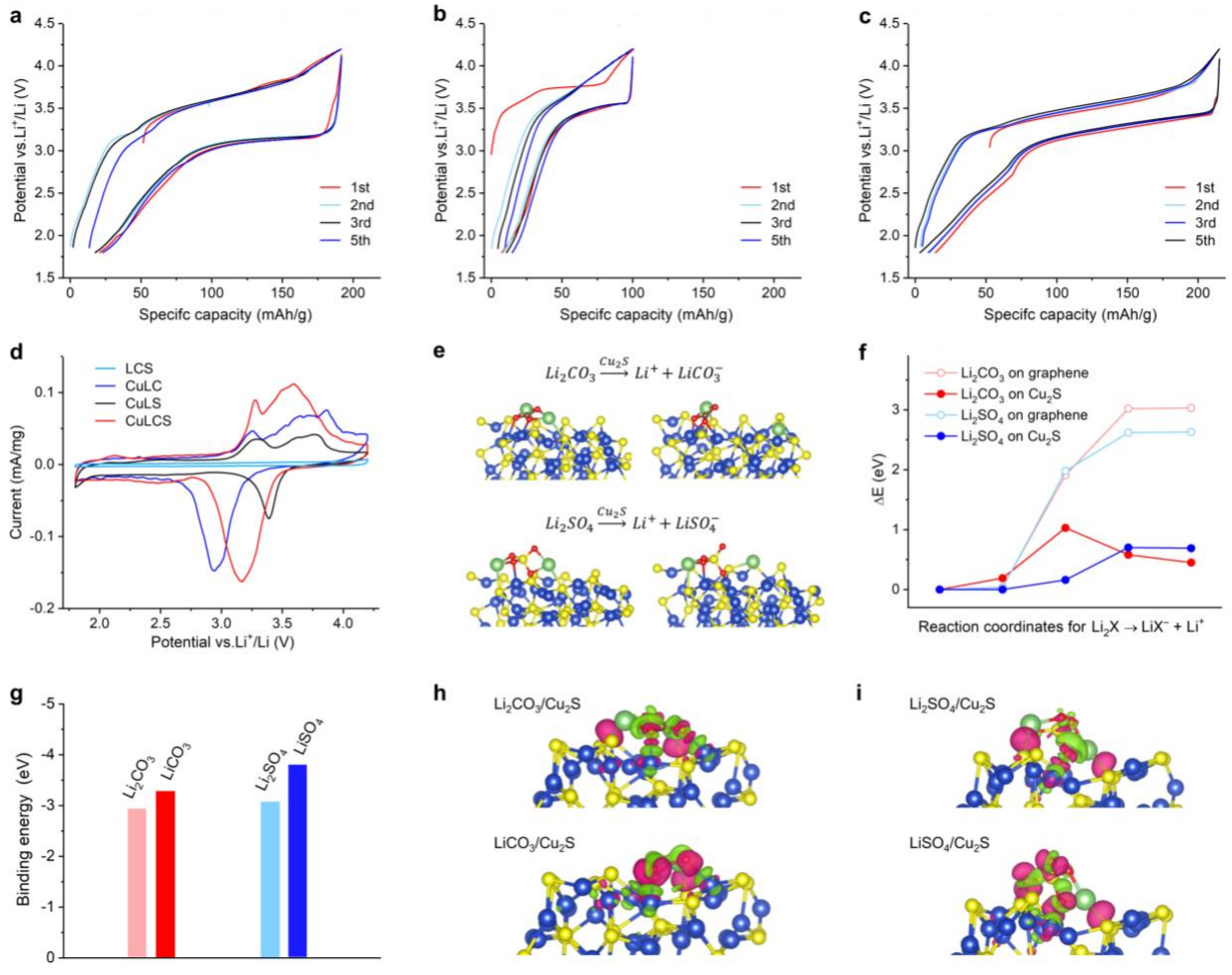

Fig. 1 | Electrochemical performance of the composite cathodes and the simulation of the interfaces of their constituents. a-c, GCD potential profiles of (a) CuLC, (b) CuLS, and (c) CuLCS at 30 mA/g. **d**, The CV curves of the LCS, CuLC, CuLS, and CuLCS electrodes at a scan rate of 0.1 mV/s. **e**, DFT-optimized atomic structures of Li_2CO_3 and Li_2SO_4 cluster models on the (111) facets of Cu_2S before and after first Li^+ dissociation (Li, green; O, red; C, gray; S, yellow; Cu, blue). **f**, Energy profiles for the first Li^+ dissociation from Li_2CO_3 and Li_2SO_4 on the (111) facets of Cu_2S and on the basal plane of graphene. **g**, Binding energies of $Li_2CO_3/LiCO_3$ and $Li_2SO_4/LiSO_4$ on the (111) facets of Cu_2S. **h**,**i**, Differential charge density distributions of $Li_2CO_3/LiCO_3$ and $Li_2SO_4/LiSO_4$ adsorbed on Cu_2S (red, electron accumulation; green, electron depletion).

The electrochemical performance of composites was evaluated by the galvanostatic charge-

discharge (GCD) cycling in coin cells, using a conventional electrolyte composed of 1 M $LiPF_6$ plus 0.1 M lithium difluoro(oxalate)borate (LiDFOB)[37], solvated in ethylene carbonate/diethyl carbonate (EC/DEC). All composite electrodes were charged first. LCS exhibits a minimal charging capacity of 10 mAh/g, which primarily originates from the capacitive ion storage of its carbon additive, KB (**Supplementary Fig. 6)**. This indicates that Li_2CO_3 and Li_2SO_4 are redox inert by the upper cutoff potential of 4.2 V (vs. Li^+/Li, and hereafter) even when they are well mixed with a conductive carbon. However, all composites containing Cu_2S—specifically CuLC, CuLS, and CuLCS—exhibited appreciable initial charge capacities and reversible discharge capacities (**Figs. 1a-c** and **Supplementary Figs. 7-9**). Notably, Cu_2S alone, when ball-milled with KB, yielded an initial charging capacity of only 10 mAh/g by an upper cutoff potential of 3.7 V. Above this potential, a cell short-circuit was observed, likely due to severe Cu^{2+} dissolution to the electrolyte and the subsequent formation of copper dendrites on the surface of the lithium counter electrode[38] (**Supplementary Fig. 10**). In the following discharge, the Cu_2S/KB electrode provides a capacity of 60 mAh/g, characterized by a plateau below 2 V, which is indicative of Li^+ insertion into the Cu_2S structure[39].

CuLC exhibits a long plateau in its initial charging potential profile with a capacity of 140 mAh/g, equivalent to extracting 0.80 Li^+ per formula unit of Li_2CO_3, as shown in **Fig. 1a**. The following discharge capacity of 171 mAh/g at an average potential of 2.9 V shows that all the first charging capacity is reversible, given that Cu_2S contributes an estimated capacity of 31 mAh/g based on its 52% mass ratio. In addition, CuLC delivers relatively stable cycling, retaining 84% of its initial capacity after 50 cycles at 30 mA/g (**Supplementary Fig. 7**). Surprisingly, CuLS also demonstrates a good capacity of 101 mAh/g in its first charging process, and a following discharge capacity of 93 mAh/g (**Fig. 1b**). Similarly, CuLS exhibits relatively stable cycling, a smaller

capacity but at a markedly higher average discharge potential of 3.2 V, as shown in **Supplementary Fig. 8**.

The next step is to assess whether the larger capacity of CuLC can be effectively integrated with the higher potential of CuLS in a single composite of Cu_2S+Li_2CO_3+Li_2SO_4 with a molar ratio of 1:1:1, featuring well-blended carbonate and sulfate anions in an amorphous phase. CuLCS shows a higher first charging capacity of 163 mAh/g from a single plateau, corresponding to 0.99 Li^+ extracted per formula unit of $Li_2(CO_3)_{1/2}(SO_4)_{1/2}$, and it delivers a capacity of 201 mAh/g at 3.0 V in the following discharge (**Fig. 1c**). In addition to exhibiting a higher capacity than CuLC and CuLS, CuLCS demonstrates a greater Coulombic efficiency for its cycling and a notably narrower potential gap of ca. 0.3 V between charge and discharge profiles, compared to that of CuLC. Importantly, all composite electrodes have a practical active mass loading of 12.5-13.0 mg/cm^2. The results suggest that CuLCS, indeed, integrates the attributes of CuLC and CuLS and exhibits a synergistic effect. The uniform plateau behavior of the charge/discharge processes of CuLCS indicates that its redox behavior stems from a homogeneous solid solution of Li_2CO_3 and Li_2SO_4, rather than their physical mixture [40, 41]. During GCD cycling, the subsequent charge/discharge profiles of CuLCS consistently overlap with those of the initial cycle, indicating the exceptional reversibility and an absence of a conditioning process usually observed for conversion electrodes[42]. Of note, CuLCS should not be considered as a conversion electrode because phase transformation cannot occur for an already-amorphous structure. Furthermore, CuLCS retains 83.7% of its initial capacity after 50 cycles at a current rate of 30 mA g^{-1} with an average Coulombic efficiency of 99.2% (**Supplementary Fig. 9**).

The cyclic voltammetry (CV) results corroborate that the anions are redox active in the presence of Cu_2S in contrast to LCS that shows no redox peaks (**Fig. 1d**). In the anodic scans, all

composites containing Cu_2S show a minor peak around 3.25 V, corresponding to the oxidation of Cu_2S, and a broad peak from 3.5 to 3.9 V, attributed to the oxidation of anions. Of note, this broad peak of CuLS reinforces the notion that Li_2SO_4 is anodically active and delithiated when coupled with Cu_2S, albeit at the lowest specific current among the composites. Interestingly, all composites exhibit a single cathodic peak, indicative of the reversible lithiation to reform Li_2CO_3 and Li_2SO_4 in the composites. Moreover, the single cathodic peak of CuLCS at 3.2 V underscores the redox behavior of a salt solid solution—$Li_2(CO_3)_{1/2}(SO_4)_{1/2}$. Results on the kinetic properties of the composite electrodes are detailed in **Supplementary Figs. 11-13**, demonstrating the benefits of anion solid solution.

The mechanism of reversible anionic oxidation in CuLCS

The superior electrochemical properties of CuLCS compared to CuLC and CuLS prompted us to elucidate the synergy between Li_2CO_3 and Li_2SO_4 in the interactions with Cu_2S. To shed light on the mechanism whereby Cu_2S facilitates the reversible redox activity of Li_2CO_3 and Li_2SO_4, we have performed density functional theory (DFT) calculations using a cluster model for the Li salts to investigate the energetics of dissociation of one Li^+. One can see that both $LiCO_3^-$ and $LiSO_4^-$ "molecules" can be well stabilized on the Cu_2S surface (**Fig. 1e**) with relatively low energy barriers for Li-ion dissociation, in contrast with the highly unfavorable energetics for the same process on graphene (**Fig. 1f**). After the oxidation process, the enhanced DFT-computed binding energies on the Cu_2S surface from Li_2CO_3 to $LiCO_3$ and from Li_2SO_4 to $LiSO_4$, as shown in **Fig. 1g**, is a result of the more charge transfer between the oxidized moieties and the Cu_2S surface: surface electrons of Cu_2S transfer to O atoms of the $LiCO_3$ and $LiSO_4$ moieties (**Fig. 1h,i**). The high binding energies stabilize the charged products—anionic radicals, thereby preventing the gas evolution of CO_2 and SO_2 and rendering the redox reactions of these anions reversible.

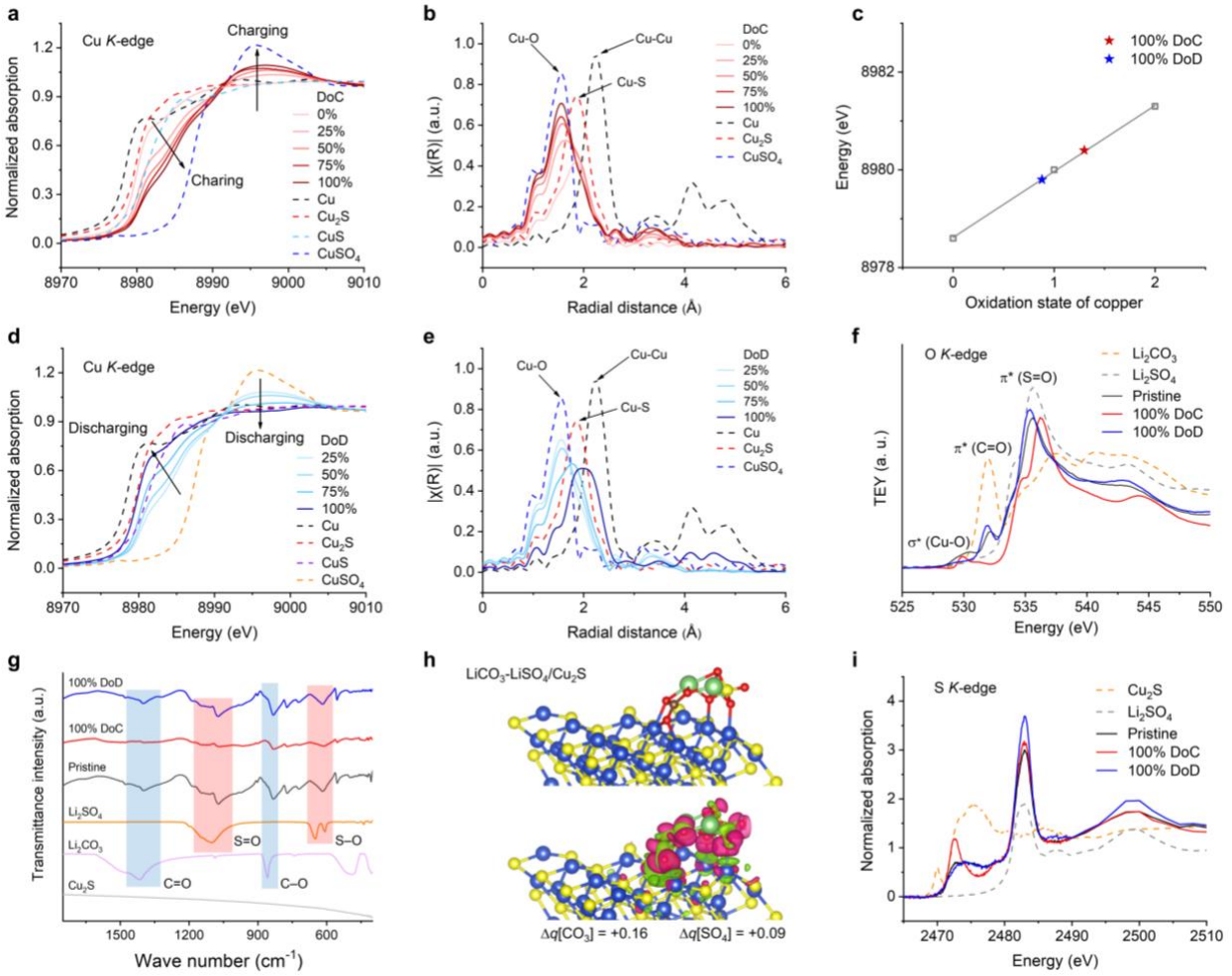

Fig. 2 | Operation mechanism of the CuLCS cathode. a, *Ex situ* Cu K-edge XANES spectra of CuLCS composite during the first charging process with varied depth of charge (DoC), and **b**, the corresponding EXAFS spectra. **c**, XANES analysis to determine the valence state of Cu in the 100% DoC and 100% DoD of CuLCS by linear fitting calibration of the Cu foil, Cu_2S, and CuS references. **d**, *Ex situ* Cu K-edge XANES spectra of CuLCS during the first discharge process with varied DoD, and **e**, the corresponding EXAFS spectra. **f**, *Ex situ* O K-edge XANES spectra, **g**, *Ex situ* FTIR spectra of the pristine, 100% DoC, and 100% DoD of CuLCS during the first cycle., **h**, Differential charge density distributions of $LiCO_3$-$LiSO_4$ "molecules" co-adsorbed on Cu_2S. **i**, *Ex situ* S K-edge XANES spectra of the pristine, 100% DoC, and 100% DoD of CuLCS during the first cycle.

Cu K-edge X-ray Absorption Near Edge Structure (XANES) results reveal that, after charging, Cu(I) in Cu_2S undergoes partial oxidation to Cu(II), reaching an average valence state of +1.3, as shown in **Fig. 2a,c** and **Supplementary Fig. 14a**. The oxidation of Cu(I) is charge-compensated by adsorption of anions[43], evidenced by the gradually intensified Cu-O correlation at 1.56 Å between Cu(II) and CO_3^{x-}/SO_4^{y-} ($0 < x, y \leqslant 2$), as observed in the Cu K-edge Extended X-ray Absorption Fine Structure (EXAFS) spectra (**Fig. 2b**). Particularly, the persistence Cu-S correlation after charging suggests that the Cu_2S local structure withstands the adsorption of anions. Upon full discharge, the oxidation state of Cu gradually returns to Cu(I), averaging at +0.9, showing only the characteristic Cu-S bond length by the 75% of the depth of discharge (DoD), (**Figs. 2c,d** and **Supplementary Fig. 14b**), suggestive of the anion desorption from the Cu_2S domains. By 100% DoD, the bond length lies between Cu-S and Cu-Cu, affirming that discharging below 2.5 V causes lithiation of Cu_2S. (**Fig. 2e**).

Do the spectroscopic results suggest the anionic redox properties of carbonate and sulfate? O K-edge X-ray absorption spectroscopy (XAS) results reveal notable changes in the O valence states of CuLCS post-charging (**Fig. 2f**). Specifically, the peak at 233 eV, associated with the C=O π^* orbital of carbonate, vanishes after full charging, suggesting the anodic oxidation of carbonate, and a minor peak at 230 eV emerges, indicative of the Cu-O σ^* bond. Concurrently, there is a blue shift in the binding energies of the S=O π^* orbital, suggesting the weakened S=O bonds and thus the loss of electron density after charging. These spectral changes in the O K-edge XAS are reversible upon Li^+ insertion in the following discharge. The Fourier transform infrared (FTIR) spectra of the CuLCS electrodes attest the redox behaviors of carbonate and sulfate. The results show the reversible disappearance and restoration of the C=O asymmetric stretches around 1402 cm^{-1}, along with the vastly weakened and restored S=O asymmetric stretches at 1071 cm^{-1}

after charge and discharge processes, respectively **(Fig. 2g)**. Indeed, the spectral results strongly support that both carbonate and sulfate ions are oxidized after charging and the fact that their oxidized states can be probed suggests that their radicals are stabilized by Cu_2S.

It appears that carbonate ions experience more substantial spectral changes, which suggests that they undergo a greater extent of oxidation than sulfate during charging, providing a larger contribution to the capacity of CuLCS. To elucidate this postulation, we simulated the delithiation process of CuLCS with a cluster model. As shown in **Fig. 2h,** when Li_2CO_3 and Li_2SO_4 clusters co-adsorbed on the surface of Cu_2S are delithiated to $LiCO_3$-$LiSO_4$, $[CO_3]$ is more oxidized than $[SO_4]$ as evidenced by the more positive charge transfer in the former. This finding is consistent with the sulfur K-edge XANES spectrum after charging (**Fig. 2i**), which, together with the O K-edge XAS results, implies that the oxidation of sulfate primarily withdraws electrons from the oxygen atoms, where the peak at 2483 eV assigned to sulfur (6+) of sulfate does not shift between 100% DoC and 100% DoD. In addition, after charging, the peak between 2470 to 2475 eV undergoes a red-shift and intensifies, as shown in **Fig. 2i**. The shift suggests a bonding between sulfide atoms with other nonmetal species, where such a bonding may come from the interactions between sulfide on the Cu_2S surface and the bound anions[44]. Upon discharge, this peak becomes broad and returns to its original binding energy.

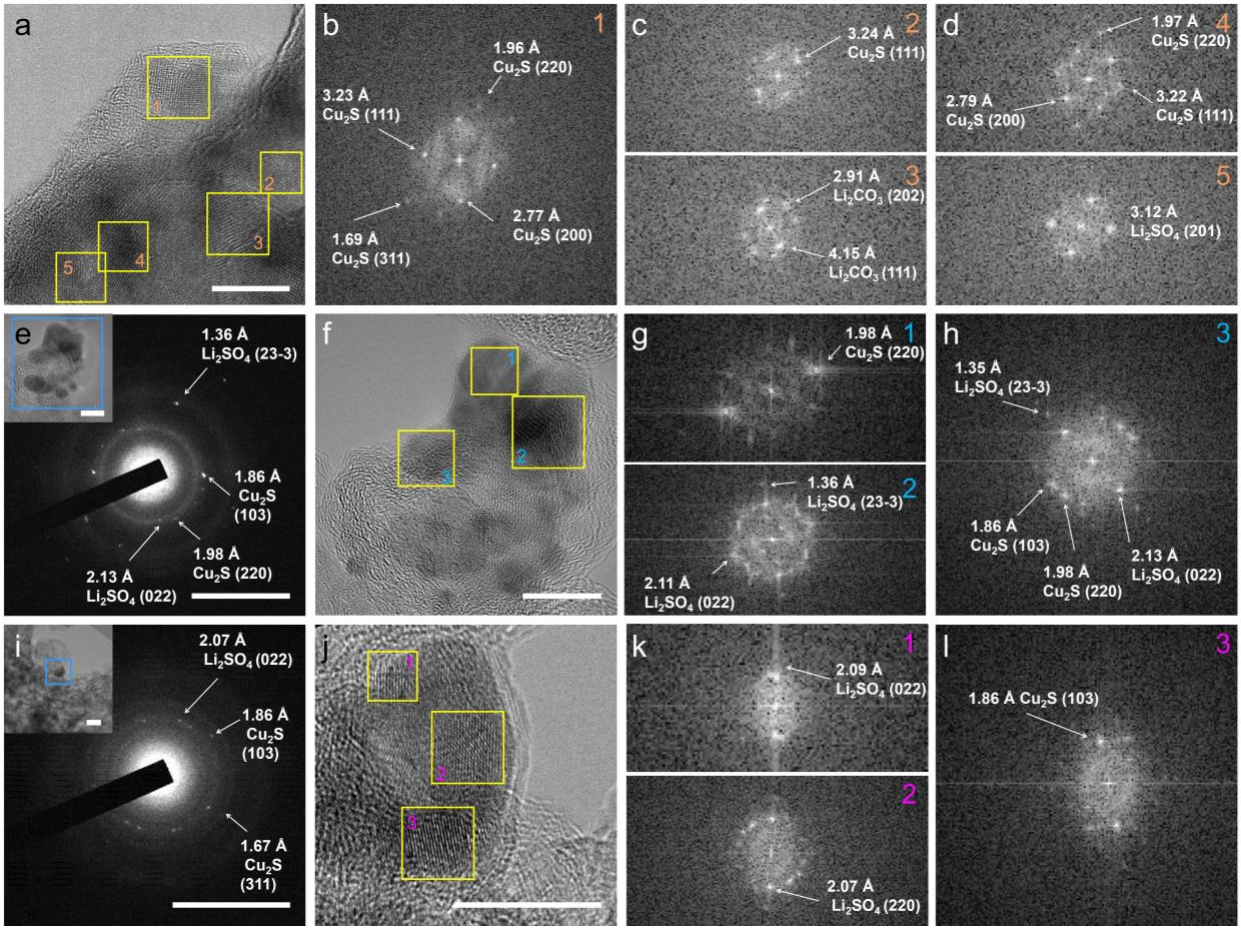

230

231 **Fig. 3. The phase evolution of the CuLCS cathode after charge and discharge in the first**
232 **cycle. a**, HRTEM image of the pristine CuLCS. Scale bar, 10 nm. **b-d**, The corresponding fast
233 Fourier-transform images of the marked regions in Fig. 3a. **e**, SAED of the marked area of the
234 inset image of charged CuLCS. Scale bars, 10 1/nm and 10 nm (Inset). **f**, HRTEM image of the
235 charged CuLCS. Scale bar, 10 nm. **g**,**h**, The corresponding fast Fourier-transform images of the
236 marked regions in Fig. 3f. **i**, SAED of the marked area of the inset image of discharged CuLCS.
237 Scale bars, 10 1/nm and 20 nm (Inset). **j**, HRTEM image of the discharged CuLCS. Scale bar, 10
238 nm. **k,l**, The corresponding fast Fourier-transform images of the marked regions in Fig. 3j.

239

240 High-resolution transmission electron microscopy (HRTEM) was used to investigate the
241 phase evolution of the CuLCS cathode after charge and discharge. **Fig. 3a-d** reveals that Cu_2S
242 nanodomains sized around 5 nm are embedded in the matrix of a largely amorphous matrix, in

which fringes of nanodomains of Li_2CO_3 and Li_2SO_4 exist sparingly. After charging, the Cu_2S and Li_2SO_4 nano-crystallites remain discernable in the composite although the d-spacings of Li_2SO_4 slightly vary in a narrow range (**Fig. 3e-h**). After discharge, fringes of Li_2SO_4 can be found besides those of Cu_2S (**Fig. 3i-l**). The microscopy results reveal that Cu_2S nanodomains intimately interface with carbonate and sulfate, and the Cu_2S lattice remains intact throughout cycling, despite the partial oxidation of Cu(I) suggested by the XANES results. Such oxidation should take place on the surface of Cu_2S domains, which does not comprise the structural integrity of these domains. Furthermore, the absence of Li_2CO_3 after full charge and discharge indicates that Li_2CO_3 experiences a deeper extent of delithiation than Li_2SO_4.

Electrochemical properties of CuLCS with Less Cu_2S

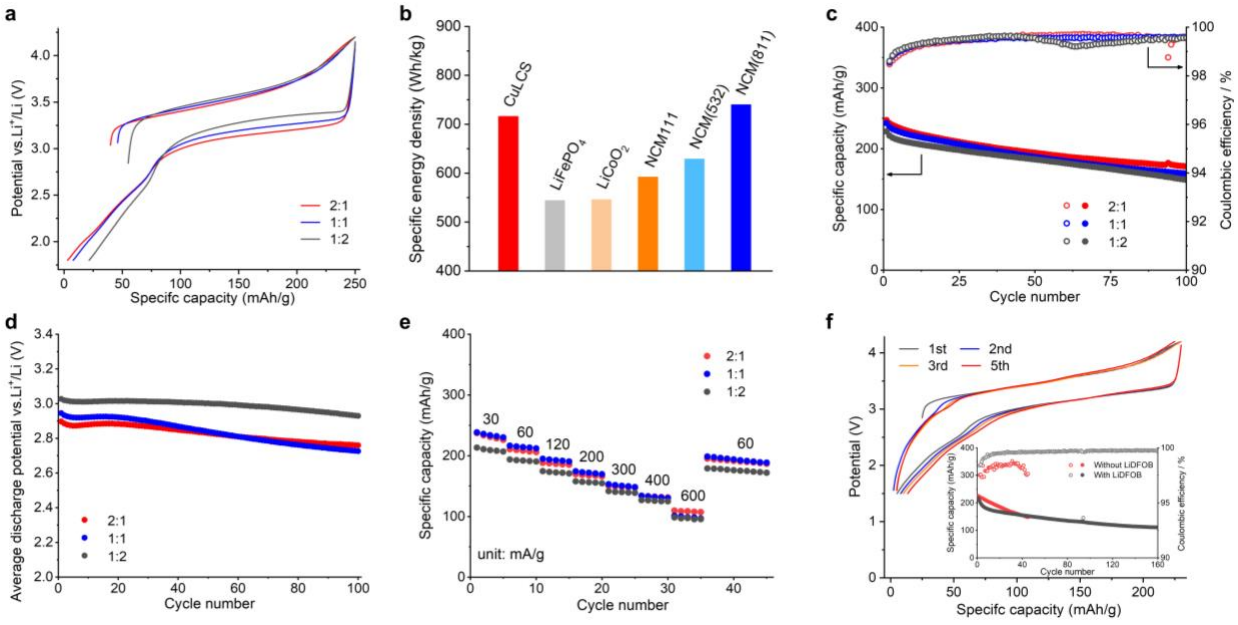

Fig. 4 | Electrochemical performances of the CuLCS cathodes with 30 wt.% Cu_2S and different molar ratios between Li_2CO_3 and Li_2SO_4. a, The GCD potential profiles of the first cycle at 30 mA/g. **b**, Specific energy of the CuLCS electrode (molar ratio 2:1, Li_2CO_3/Li_2SO_4),

compared with commercial LIB cathode materials. **c**, Cycling performance at 30 mA/g. **d**, Average discharge potentials of CuLCS electrodes during 100 cycles at 30 mA/g. **e**, Rate capability of CuLCS electrodes. **f**, The GCD profiles of the CuLCS (molar ratio 2:1, Li_2CO_3/Li_2SO_4) || graphite full cell at 30 mA/g with the N/P ratio of 1:1.2 and 1 M $LiPF_6$ in EC/DEC (1:1, v/v) as the electrolyte. Inset: cycling of the full cells in the electrolyte of 1 M $LiPF_6$ in EC/DEC (1:1, v/v) with and without 0.1 M LiDFOB.

The spectral results suggest the redox behaviors of Cu(I) of Cu_2S, raising questions about the exact role of Cu_2S: Does it serve as a primary active mass besides being a binding agent? To test this, we postulate that if Cu_2S is not a primary active mass, reducing its percentage should enhance the capacity of the CuLCS electrode when the necessary interfacing between Cu_2S and lithium salts is not compromised. Thus, we decreased the mass percentage of Cu_2S from 46% to 30%. As **Fig. 4a** shows, the composite with 30% Cu_2S exhibits a higher first charge/discharge capacities of 204/242 mAh/g at 30 mA/g with an average discharge potential of 2.95 V (**Supplementary Fig. 15a**). The improved capacities with less Cu_2S content unequivocally support the notion that Cu_2S serves mainly as a binding agent, albeit its capacity contribution may not be negligible, and the anions are the predominant active mass. However, when the percentage of Cu_2S is further reduced to 20%, the first charge/discharge capacities decrease to 173/187 mAh/g (**Supplementary Fig. 16**), which suggest the critical role of Cu_2S in the composites to provide the binding interface to induce the redox reactivity of lithium salts.

Further exploring the impact of anion ratios on performance, we varied the Li_2CO_3/Li_2SO_4 molar ratios from 1:1 to 2:1 and 1:2, resulting in the first charge/discharge capacities of 210/247 mAh/g and 195/229 mAh/g, respectively, accompanied by average discharge potentials of 2.90 and 3.03 V (**Supplementary Figs. 15b,c**). The results indicate a trade-off between specific

capacity and average discharge potential, influenced by the varying ratios of Li_2CO_3 and Li_2SO_4. Higher Li_2CO_3 content promotes the specific capacity, while more Li_2SO_4 improves the average discharge potential and reduces the extent of polarization. Nevertheless, the fact that the sulfate-rich composite can delithiate 1.02 Li^+ per unit formula of $Li_2(CO_3)_{1/3}(SO_4)_{2/3}$, corresponding to the first charging capacity of 195 mAh/g, further corroborates the anodic redox reactivity of sulfate in the presence of Cu_2S.

Notably, the electrode with the Li_2CO_3/Li_2SO_4 molar ratio of 2:1 achieves a specific energy of 716 Wh/kg, comparable to that of the Ni/Co-based layered oxide cathodes (**Fig. 4b**)[2]. Moreover, CuLCS composites with different Li_2CO_3/Li_2SO_4 ratios exhibited similar respective capacity retentions of 69.2%, 65.7%, and 65.1% after 100 cycles at 30 mA/g (**Fig. 4c**). Of note, their average discharge potentials maintain 95.3%, 92.5%, and 96.8% of the initial values after 100 cycles, suggestive of the reversible nature of the anionic reactions and an absence of gas evolution (**Fig. 4d**). Furthermore, the CuLCS electrodes exhibit promising rate capability across the different molar ratios (**Fig. 4e**).

In the extension to the full cell studies, we evaluated the performance of CuLCS (30 wt.% Cu_2S, Li_2CO_3/Li_2SO_4 molar ratio of 2:1), paired with a graphite anode (**Supplementary Fig. 17**), with an anode/cathode capacity (N/P) ratio of 1/1.2. The graphite anode has been pre-discharged to 20% DoD. The full cell delivers an initial discharge capacity of 217 mAh/g at an average potential of 2.89 V at 30 mA/g and relative stable cycling performance (**Fig. 4f**). The results show that the 0.1 M LiDFOB additive in the electrolyte of 1 M $LiPF_6$ EC/DEC (1:1, v/v) helps retain the high Coulombic efficiency. Notably, the full-cell performance was obtained with an active mass loading of ~10 mg/cm^2 for the composite electrodes, underscoring its considerable promise for practical applications.

Conclusions

In this study, we demonstrate that common lithium salts, specifically Li_2CO_3 and Li_2SO_4, can serve effectively as cathode materials in Li-ion batteries with practical active mass loading, when finely mixed Cu_2S as a binding agent. This configuration enables both Li_2CO_3 and Li_2SO_4 to undergo reversible delithiation, where Cu_2S plays a crucial role in inducing their reactivity and stabilizing the oxidized anionic radicals formed from carbonate and sulfate. Our results highlight that the solid solution of the two anions significantly enhances the battery's performance by increasing the overall capacity, reducing polarization, and improving Coulombic efficiency, delivering the performance comparable to commercial nickel/cobalt-based oxide cathodes. Our findings provide opportunities for utilizing abundant lithium salts as sustainable cathode materials in Li-ion batteries, offering a promising avenue for advancing energy storage technologies.

Methods

Materials preparation

The CuLC, CuLS, CuLCS, and LCS composites were prepared with Li_2CO_3 (Fluka), Li_2SO_4 (ACROS ORGANICS), Cu_2S (Sigma-Aldrich), and KetjenBlack carbon (EC600JD, MSE Supplies) without any prior purification. Li_2CO_3 and Cu_2S, Li_2SO_4 and Cu_2S, Li_2CO_3, Li_2SO_4, and Cu_2S, or Li_2CO_3 and Li_2SO_4 in the molar ratios of 2:1, 2:1, 1:1:1, and 1:1, respectively, were added to a planetary ball mill (Pulverisette® 6; Fritsch International, Pittsboro, NC) along with additional 5.9 wt.% KetjenBlack carbon. The mixtures were sealed in an Ar-filled glovebox with H_2O and O_2 concentrations below 0.1 ppm. The mixtures in the bowl were subjected to ball milling at 400 r.p.m. for 50 hours, with a 5-minute break every 30 minutes. For comparison, pure Cu_2S was also mixed with KetjenBlack carbon in the same mass ratio as the above composites, then the mixture was sealed in an Ar-filled glovebox and ball-milled under same conditions. The CuLCS with the lower mass ratio of Cu_2S (30 wt.% and 20 wt.%) were prepared in the same way as the aforementioned CuLCS, and the mass ratios between Cu_2S and the lithium salts are 3:7 and 1:4.

Graphite anode was purchased from MTI Corporation, which comprises graphite, conductive carbon (Super P) and binder (SBR+CMC, 2.5% SBR, 1.8% CMC) in a weight ratio of 93.2:4.3:2.5 with copper foil (9 micron) as the current collector.

Electrochemical measurements

The working electrode is composed of 85 wt.% active materials (CuLC, CuLS, CuLCS, LCS, or Cu_2S), 10 wt.% KetjenBlack carbon, and 5 wt.% polytetrafluoroethylene (PTFE, Sigma-Aldrich) binder. These materials are extruded to form a free-standing film, which is then punched into discs, 12 mm in diameter. Li foil is used as the counter and reference electrode. For CuLC, CuLS, and Cu_2S electrodes, glass microfiber filter membranes (Whatman, Grade GF/F) are used as separators, while Celgard 2500 is used for CuLCS and LCS electrodes. The mass loading of all electrodes for half cells is approximately 12.5-13.0 mg/cm^2, and the specific capacity is calculated based on the total mass of Cu_2S plus lithium salts. An electrolyte of 1 M $LiPF_6$ plus 0.1 M LiDFOB in EC/DEC (1:1 by volume) is used for all half cells. For full cells with graphite as the anode, 1 M $LiPF_6$ in EC/DEC (1:1 by volume) with and without 0.1 M LiDFOB are employed as electrolytes. The cells are assembled in an Ar-filled glovebox with H_2O and O_2 concentrations below 0.1 ppm. We tested the electrochemical performance of the cathodes on a Landt CT3002A battery testing system at various current rates and a temperature of 30 °C. The cutoff potential window was set to 1.8-4.2 V vs. Li^+/Li for half cells. For CuLCS || graphite full cells, the voltage was set to 1.5-4.2 V. Cyclic voltammetry (CV) was tested on a VMP-3 multichannel workstation at a scan rate of 0.1-0.5 mV/s. To prepare the full cells, we set the N/P ratio to 1.2. The specific capacity of the cathodes was based on the initial charging specific capacity. The mass loading of CuLCS for full cells is ca. 10 mg/cm^2. We prelithiated the graphite anode to 20% DoD to compensate for the extra lithium required for discharging to 1.5 V. The graphite anodes were run for 10 cycles before assembling the full cells to stabilize the interface.

We conducted the galvano electrochemical impedance spectroscopy (GEIS) test using a VMP-3 electrochemical workstation (BioLogic). The coin cells were precycled once at 30°C (1.8 to 4.2 V, 30 mA/g) before performing the GEIS test at 30°C. After resting for 3 hours, galvanostatic charge-discharge (GCD) cycling was carried out at 30 mA/g with direct current (DC) inputs. During the GCD process, EIS measurements were conducted by adding alternating current (AC)

signals of ±10 mA/g amplitude to the DC signal. To minimize the impact of AC signals on cell cycling, we included 15-minute intervals between each EIS measurement. The frequency range was set from 200 kHz to 2 Hz, with each measurement taking approximately 27 seconds. We performed DRT analysis on each EIS dataset using MATLAB-based DRT tools developed by Wan et al., applying the default parameters to calculate $\gamma(\ln \tau)$ versus τ.

Physical characterization

XAS for the Cu K edge was performed at 7-BM beamline of National Synchrotron Light Source II (NSLS-II) in Brookhaven National Laboratory. All the samples were sealed in Kapton tape before testing. The data analysis is conducted by Athena software package. Sulfur K-edge XANES spectra of CuLCS samples and reference materials were collected at beamline 14-3 at the Stanford Synchrotron Radiation Light source (SSRL) in a He atmosphere. A 7-element vortex detector was used to monitor the fluorescence signal. The calibration of the monochromator was obtained by adjusting the maximum energy of the pre-edge feature of sodium thiosulfate to 2472.02 eV. O K edge Soft XAS measurements were conducted at the elliptically polarizing undulator (EPU) beamline 13-3 at SSRL. The electrodes were extracted from coin cells containing liquid electrolyte and subsequently dried to enable soft X-ray measurements in an ultra-high vacuum environment. The incident beam was monochromatized using a 600-lines/mm spherical grating monochromator, with its angle set at 30 degrees relative to the sample surface.

X-ray diffraction (XRD) patterns were collected on a Rigaku Ultima IV diffractometer with the Cu Kα radiation (λ = 1.5406 Å). The microstructure and morphology were evaluated by using FEI NOVA 230 field-emission scanning electron microscopy (FESEM). Transmission electron microscopy (TEM) images and its corresponding energy-dispersive X-ray spectroscopy (EDS) of the composite were collected on a FEI Titan 80-300 high-resolution transmission electron microscopy with four embedded Bruker SDD detectors. TEM (JEOL-JEM 2100F) equipped with energy-dispersive spectroscopy (EDS, Bruker X-Flash 6/60 series) was used for the HRTEM/SAED. To prepare the samples, the electrodes recovered from the cycled cells were washed and ultrasonically dispersed in cyclohexane for 1 hour. The dispersion was dropped onto a Ni mesh to avoid any influence from Cu. All the samples were vacuum dried before characterization. FTIR spectra were recorded using a PerkinElmer Spectrum Two attenuated total reflection analyzer.

Computational methods

Density functional theory calculations were performed using the Vienna ab initio simulation package (VASP)[45,46] with periodic boundary conditions. The interaction between the electrons and the nucleus was described by the projector augmented wave (PAW) method[47,48] with an energy cutoff of 500 eV. The Perdew-Burke-Ernzerhof (PBE) functional of the generalized gradient approximation (GGA) was used for electron exchange-correlation[49]. Monkhorst-Pack *k*-point sampling with the *k*-point spacing <0.03 $Å^{-1}$ was used. The dispersion forces were included with the DFT-D3 method[50]. Spin polarization was enabled in all the calculations.

Cu_2S slab models were built from the tetragonal copper sulfide[51] with 4 atomic layers for the (111) surface, which has the lowest energy[52]. A vacuum region of 20 Å along the *z*-direction was applied in each slab model. The top two layers of the slab models and the adsorbates were allowed to relax until the forces on each atom is less than 0.02 eV/Å, while the bottom two layers were fixed during geometry optimization. The climbing-image nudged elastic band (CI-NEB) method[53] was used to determine the transition states for the dissociation of Li_2CO_3 and Li_2SO_4 on Cu_2S surface. Bader charge analysis was employed to obtain the partial atomic charges in the slab models[54].

Acknowledgements

X.J., D.J., and C.W. thank for the financial support from U.S. Department of Energy (DOE), Basic Energy Science Program, Award No. DE-SC0023408. X.J. is grateful for the financial support from the U.S. National Science Foundation, Award Number: CBET-2215645. This research employed the Advanced Light Source, a DOE Office of Science User Facility under a contract No. DE-AC02-05CH11231. This work acknowledges support from the U. S. DOE, Office of Energy Efficiency and Renewable Energy, Vehicle Technologies Office. Argonne National Laboratory is operated for DOE Office of Science by UChicago Argonne, LLC, under contract number DE-AC02-06CH11357. Use of the National Synchrotron Light Source II (7-BM) is supported by the U.S. DOE, an Office of Science user Facility operated by Brookhaven National Laboratory under

contract number DE-SC0012704. Use of the Stanford Synchrotron Radiation Light source, SLAC National Accelerator Laboratory, is supported by the U.S. DOE, Office of Science, Office of Basic Energy Sciences under Contract No. DE-AC02-76SF00515.

Author contributions

X.J. conceived the project. X.J. and M.J. designed the research. X.J., D.J., X.Z., T.L., and C.W. supervised the research. M.Y. led electrochemical experiments and analysis. B.L. and D.J. conducted computation; J.W., Z.X., Y.C., M.K., G.F., Y.Y., A.S., Z.Z. A.K.Y. K.S., W.Y., Y.L., T.O.P. T.L., and X.Z. contributed to spectral characterization. M.S.J., Y.S., and M.L. conducted experiments. Y.X., N.Z., C.W., and C.W. contributed to microscopy studies. All authors discussed the results and contributed to data interpretation and paper revisions.

Competing interests

X.J. and M.Y. are inventors for a US patent application no. 18/510,483 (pending), filed by Oregon State University on November 15th 2023. The authors do not declare other competing interests.

Data availability

Data supporting the findings of this study are included in the paper and the Supplementary Information. Raw data are available from corresponding authors upon request.

References

1 Li, H. *et al.* Is cobalt needed in Ni-rich positive electrode materials for lithium ion batteries? *J. Electrochem. Soc.* **166**, A429-A439 (2019).

2 Zeng, X. *et al.* Commercialization of lithium battery technologies for electric vehicles. *Adv. Energy Mater.* **27**, 1900161 (2019).

3 Baars, J., Domenech, T., Bleischwitz, R., Melin, H. E. & Heidrich, O. Circular economy strategies for electric vehicle batteries reduce reliance on raw materials. *Nat. Sustain.* **4**, 71–79 (2021).

4 Turcheniuk, K., Bondarev, D., Amatucci, G. G. & Yushin, G. Battery materials for low-cost

electric transportation. *Mater. Today* **42**, 57-72 (2021).
5 Liu, D. *et al.* Controlled large-area lithium deposition to reduce swelling of high-energy lithium metal pouch cells in liquid electrolytes. *Nat. Energy* **9**, 559–569 (2024).
6 Yuan, X., Liu, B., Mecklenburg, M. & Li, Y. Ultrafast deposition of faceted lithium polyhedra by outpacing SEI formation. *Nature* **620**, 86-91 (2023).
7 Li, Y. *et al.* Atomic structure of sensitive battery materials and interfaces revealed by cryo–electron microscopy. *Science* **358**, 506-510 (2017).
8 Chen, Y. *et al.* Unlocking Li superionic conductivity in face-centred cubic oxides via face-sharing configurations. *Nat. Mater.* **23**, 535-542 (2024).
9 Wu, F., Fitzhugh, W., Ye, L., Ning, J. & Li, X. Advanced sulfide solid electrolyte by core-shell structural design. *Nat. Commun.* **9**, 4037 (2018).
10 Padhi, A. K., Nanjundaswamy, K. S. & Goodenough, J. B. Phospho-olivines as Positive-Electrode Materials for Rechargeable Lithium Batteries. *J. Electrochem. Soc.* **144**, 1188-1194 (1997).
11 Huang, H., Yin, S. C. & Nazar, L. F. Approaching theoretical capacity of $LiFePO_4$ at room temperature at high rates. *Electrochem. Solid-State Lett.* **4**, A170–172 (2001).
12 Masquelier, C. & Croguennec, L. Polyanionic (phosphates, silicates, sulfates) frameworks as electrode materials for rechargeable Li (or Na) batteries. *Chem. Rev.* **113**, 6552-6591 (2013).
13 Gent, W. E. *et al.* Coupling between oxygen redox and cation migration explains unusual electrochemistry in lithium-rich layered oxides. *Nat. Commun.* **8**, 2091 (2017).
14 Xu, J. *et al.* Elucidating anionic oxygen activity in lithium-rich layered oxides. *Nat. Commun.* **9**, 947 (2018).
15 Liu, T. *et al.* Origin of structural degradation in Li-rich layered oxide cathode. *Nature* **606**, 305-312 (2022).
16 Lee, J. *et al.* Reversible Mn^{2+}/Mn^{4+} double redox in lithium-excess cathode materials. *Nature* **556**, 185–190 (2018).
17 Eum, D. *et al.* Voltage decay and redox asymmetry mitigation by reversible cation migration in lithium-rich layered oxide electrodes. *Nat. Mater.* **19**, 419-427 (2020).
18 Zhou, G., Paek, E., Hwang, G. S. & Manthiram, A. Long-life Li/polysulphide batteries with high sulphur loading enabled by lightweight three-dimensional nitrogen/sulphur-codoped graphene sponge. *Nat. Commun.* **6**, 7760 (2015).
19 Pang, Q. *et al.* Tuning the electrolyte network structure to invoke quasi-solid state sulfur conversion and suppress lithium dendrite formation in Li–S batteries. *Nat. Energy* **3**, 783-791 (2018).
20 Zhou, G. *et al.* Supercooled liquid sulfur maintained in three-dimensional current collector for high-performance Li-S batteries. *Sci. Adv.* **6**, eaay5098 (2020).
21 Zhou, J. *et al.* Healable and conductive sulfur iodide for solid-state Li–S batteries. *Nature* **627**, 301-305 (2024).
22 Suo, L., Hu, Y.-S., Li, H., Armand, M. & Chen, L. A new class of solvent-in-salt electrolyte for high-energy rechargeable metallic lithium batteries. *Nat. Commun.* **4**, 1481 (2013).
23 Ahn, S. *et al.* Why charging Li–air batteries with current low-voltage mediators is slow and singlet oxygen does not explain degradation. *Nat. Chem.* **15**, 1022-1029 (2023).
24 Qiao, Y., Jiang, K., Deng, H. & Zhou, H. A high-energy-density and long-life lithium-ion battery via reversible oxide–peroxide conversion. *Nat. Catal.* **2**, 1035-1044 (2019).
25 Zhu, Z. *et al.* Anion-redox nanolithia cathodes for Li-ion batteries. *Nat. Energy* **1**, 16111 (2016).

26 Xie, C. *et al.* Reversible multielectron transfer I−/IO3− cathode enabled by a hetero-halogen electrolyte for high-energy-density aqueous batteries. *Nat. Energy* https://doi.org/10.1038/s41560-024-01515-9 (2024).
27 Yang, C. *et al.* Aqueous Li-ion battery enabled by halogen conversion–intercalation chemistry in graphite. *Nature* **569**, 245-250 (2019).
28 Zhu, G. *et al.* Rechargeable Na/Cl_2 and Li/Cl_2 batteries. *Nature* **596**, 525-530 (2021).
29 Cao, W., Zhang, J. & Li, H. Batteries with high theoretical energy densities. E*nergy Storage Mater.* **26**, 46-55 (2020).
30 Li, C. *et al.* Li_2CO_3 nanocomposites as cathode lithium replenishment material for high-energy-density Li-ion batteries. *ACS Appl. Mater. Interfaces* **15**, 44921-44931 (2023).
31 Zhu, Y. *et al.* Lattice engineering on Li_2CO_3-based sacrificial cathode prelithiation agent for improving the energy density of Li-ion battery full-cell. *Adv. Mater.* **36**, 2312159 (2023).
32 Schmuch, R., Wagner, R., Hörpel, G., Placke, T. & Winter, M. Performance and cost of materials for lithium-based rechargeable automotive batteries. *Nat. Energy* **3**, 267–278 (2018).
33 Zhao, S. *et al.* Mechanism and modelling of reactive crystallization process of lithium carbonate. *Processes* **7**, 248 (2019).
34 Dissanayake, M. A. K. L. & Mellander, B. E. Phase diagram and electrical conductivity of the Li_2SO_4-Li_2CO_3 system. *Solid State Ionics* **21**, 279-285 (1986).
35 Shin, Y.-U. *et al.* Electrochemical oxidation of organics in sulfate solutions on boron-doped diamond electrode: Multiple pathways for sulfate radical generation. *Appl. Catal. B: Environ.* **254**, 156-165 (2019).
36 Mu, X., Pan, H., He, P. & Zhou, H. Li–CO_2 and Na–CO_2 batteries: Toward greener and sustainable electrical energy storage. *Adv. Mater.* **32**, 1903790 (2020).
37 Xu, K. Interfaces and interphases in batteries. *J. Power Sources* **559**, 232652 (2023).
38 Yu, M. *et al.* Reversible copper cathode for nonaqueous dual-ion batteries. *Angew. Chem. Int. Ed.* **61**, e202212191 (2022).
39 Jiang, K., Chen, Z. & Meng, X. CuS and Cu_2S as cathode materials for lithium batteries: A review. *ChemElectroChem* **6**, 2825-2840 (2019).
40 Lu, J., Nishimura, S.-i. & Yamada, A. Polyanionic solid-solution cathodes for rechargeable batteries. *Chem. Mater.* **29**, 3597-3602 (2017).
41 Kim, H. *et al.* New iron-based mixed-polyanion cathodes for lithium and sodium rechargeable batteries: combined first principles calculations and experimental study. *J. Am. Chem. Soc.* **134**, 10369-10372 (2012).
42 Wang, L. *et al.* Li-free cathode materials for high energy density lithium batteries. *Joule* **3**, 2086-2102 (2019).
43 Yu, M. et al. Unlocking iron metal as a cathode for sustainable Li-ion batteries by an anion solid-solution. *Sci. Adv.* **10**, eadn4441 (2024).
44 Kumar, P., Nagarajan, R. & Sarangi, R. Quantitative X-ray absorption and emission spectroscopies: electronic structure elucidation of Cu_2S and CuS. *J. Mater. Chem. C* **1**, 2448-2454 (2013).
45 Kresse, G. & Furthmüller, J. Efficiency of ab-initio total energy calculations for metals and semiconductors using a plane-wave basis set. *Comput. Mater. Sci.* **6**, 15-50 (1996).
46 Kresse, G. & Furthmüller, J. Efficient iterative schemes for ab initio total-energy calculations using a plane-wave basis set. *Phys. Rev. B* **54**, 11169-11186 (1996).
47 Kresse, G. & Joubert, D. From ultrasoft pseudopotentials to the projector augmented-wave method. *Phys. Rev. B* **59**, 1758-1775 (1999).

48 Blöchl, P. E. Projector augmented-wave method. *Phys. Rev. B* **50**, 17953-17979 (1994).
49 Perdew, J. P., Burke, K. & Ernzerhof, M. Generalized gradient approximation made simple. *Phys. Rev. Lett.* **77**, 3865-3868 (1996).
50 Grimme, S., Antony, J., Ehrlich, S. & Krieg, H. A consistent and accurate ab initio parametrization of density functional dispersion correction (DFT-D) for the 94 elements H-Pu. *J. Chem. Phys.* **132**, (2010).
51 Zimmer, D. *et al.* Phase transition of tetragonal copper sulfide Cu_2S at low temperatures. *Phys. Rev. B* **96**, 054108 (2017).
52 Kim, M.-C. *et al.* Hydrogen bonding-mediated enhancement of bioinspired electrochemical nitrogen reduction on $Cu_{2-x}S$ catalysts. *ACS Catal.* **10**, 10577-10584 (2020).
53 Henkelman, G., Uberuaga, B. P. & Jónsson, H. A climbing image nudged elastic band method for finding saddle points and minimum energy paths. *J. Chem. Phys.* **113**, 9901-9904 (2000).
54 Henkelman, G., Arnaldsson, A. & Jónsson, H. A fast and robust algorithm for Bader decomposition of charge density. *Comput. Mater. Sci.* **36**, 354-360 (2006).